



TECHNICAL ARTICLE

Study on Friction Properties of In Situ Synthesized (AlB₂ + Al₂O₃)/A356 Composite

Lei Jiao, Zhiwen Wang , Yutao Zhao, Fan Li, Baowang Wang, Hui Li, Chengyong Xu, Qinjun Zhang, and Sheretskyi Volodymyr

Submitted: 13 February 2023 / Revised: 23 May 2023 / Accepted: 26 May 2023 / Published online: 12 June 2023

In this paper, we designed the A356-B₂O₃-KBF₄ reaction system to synthesize (AlB₂ + Al₂O₃)/A356 biphasic particles-reinforced aluminum matrix composite with varying weight percentages (2%, 4%, 6%, and 8%). The synthesis was achieved through mechanical mixing and mixed salt reaction. We studied the friction and wear performance of the composite at room temperature using XRD, PC, SEM, EDS, laser confocal microscopy, and microhardness analysis. Our results indicate that the AlB₂ and Al₂O₃ duplex-enhanced particles were effectively synthesized, with predominantly short rod morphology and local clustering observed for the AlB₂ particles. The AlB₂ particles were mostly in the micron-scale range, while the Al₂O₃ particles were mostly in the nanoscale range, both exhibiting agglomeration phenomena. Both enhanced particles showed an agglomeration phenomenon and could grow together with the interface binding very closely. At 6 wt.% mass fraction of biphasic particles, the composite exhibited the best refinement effect on-Al grains, as well as the greatest friction reduction effect and wear resistance for both the (AlB₂ + Al₂O₃)/A356 composite and the A356 matrix alloy. The wear mechanism was primarily abrasive wear, while the A356 matrix alloy's wear mechanism was adhesive wear.

Keywords A356-B₂O₃-KBF₄ system, composite material, duplex particles, friction and wear behavior

1. Introduction

Particulate-reinforced aluminum matrix composites are widely used and have significant advantages compared with fiber-reinforced aluminum matrix composites [1-3], such as isotropic nature, simple preparation process, and low cost [4-6]. The PAMCs (particulate aluminum matrix composites) have a higher specific strength, specific stiffness, and wear resistance than the aluminum alloy matrix [7-9]. However, in situ PAMCs have advantages over external PAMCs, such as clean interface and low process cost [10-12]. With the deepening of the research, the preparation cost of aluminum in situ PAMCs is still decreasing, so the in situ PAMCs can meet the requirements of lightweight, good designability, and low preparation cost [13-16]. This allows aluminum in situ PAMCs to have broad applications in both the military and civilian sectors,

especially in the vehicles, aerospace, and electronic packaging industries [17, 18]. Because of the excellent friction wear properties, in situ PAMCs have become the focus of many researchers of friction wear behavior recently [19-22]. However, due to the choice of the matrix material, particle type, friction wear working temperature, experimental external load, and sliding speed will be studied on the friction wear behavior of composite materials which have different degrees and the mutual influence between the complexity of PAMCs [23-28].

In situ particles as enhanced phase will be evenly distributed in the aluminum substrate, such as coarse particles [29, 30], so many researchers add external field auxiliary reaction in the process of in situ particle reaction to study the influence of external field on particle morphology and distribution. The standard methods include mechanical stirring, electromagnetic stirring, high-energy ultrasonic field, etc [31-33].

Particle-reinforced aluminum matrix composite is a composite material that uses aluminum and its alloy as the matrix and is enhanced by external addition or internal in situ reaction [34-37]. The related research of single particle-reinforced aluminum matrix composite material has matured.

Successful particle-reinforced aluminum-based composite of AlB₂ prepared by powder metallurgy and the hot rolling process by Han et al. [38], and others found that AlB₂ particles generated in situ significantly improved the wear resistance of pure Al. The wear area and friction coefficient of the samples also increased linearly with increasing load. The addition of AlB₂ has a significant reduction effect. Hidalgo-Hernandez et al. [39] similarly prepared the AlB₂ particle-reinforced aluminum-based composite material and found that the material achieved the highest wear resistance when the AlB₂ particle content was 4 wt%. The analysis of oxidation wear, particle wear, and peeling wear. AlB₂ particles play a direct role in the wear behavior of composite material. Because the increase of

Lei Jiao, Zhiwen Wang, Yutao Zhao, Fan Li, Baowang Wang, Chengyong Xu, and Qinjun Zhang, School of Materials Science and Engineering, Jiangsu University, Zhenjiang 212013, People's Republic of China; Hui Li, School of Materials Science and Engineering, Jiangsu university of science and technology, Zhenjiang 212003, People's Republic of China; and Sheretskyi Volodymyr, Institute of Physics and Technology of Metals and Alloys, National Academy of Sciences of Ukraine, Kyiv, Ukraine. Contact e-mails: jiaolei@ujs.edu.cn, 1443305211@qq.com, zhaoyt@ujs.edu.cn, lifan970814@163.com, w20154610110@163.com, lihuiwind@163.com, 1745953098@qq.com, 1353983839@qq.com, and 13952809001@163.com.

boron content affects the wear behavior of composite material, the wear resistance of composite material is obtained.

Bai et al. [40] prepared 7075 aluminum matrix composite by mechanical alloying mechanism and the pressing sintering method and found that when the mass fraction of Al_2O_3 particles reached 5%, the friction wear performance got the composite. With the slight wear mechanism at room temperature, it can be seen that the addition of Al_2O_3 can enhance the wear resistance of the material. Yang et al. [41] found that when the Al_2O_3 particles are nanoscale, the wear rate and friction coefficient are reduced, while the particle size increases the degree of wear and thus reduces the wear resistance of the material.

Muraliraja and Wu et al. have studied the particles of single SiC particles or single alumina particles-reinforced aluminum-based composites. Many problems were also found in the course of related studies [42, 43]. For example, a single enhanced particle cannot meet the requirements of improving multiple properties of the material, and the limitations of the single enhanced particle mass fraction cannot be broken through [44-46]. In terms of conventional performance, the successfully synthesized bipolar particle-reinforced aluminum matrix composite is significantly better than the single particles. Narendra et al. [47] studied ZrB_2 particle-reinforced aluminum matrix. They found that the hardness and strength increased with the increase in the total amount of particles, but as the upper limit of reinforced particles was reached, the performance was difficult to improve. Zhu et al. [48] study also introduced ZrB_2 particles-reinforced aluminum at the same time- Al_2O_3 particles and thus found that biphasic particles enhanced composite than a single ZrB_2 particle, strength has increased significantly, and using the identical synthesis method, biphasic particles have higher particle mass fraction limit, and performance improvement limit also increased. Biphasic particles have more advantages than single particles [49, 50]. Biphasic particles can not only increase enhanced species to make up for the lack of other performance or play synergy to improve some performance further and can through different reaction systems avoid thermodynamic dynamics, thus significantly improving composite in situ enhanced particle mass fraction, and can even achieve the effect of refining enhanced particles. There is a significant development space to improve the friction performance of materials [51].

Due to the in situ effects caused by the addition of enhanced nanoparticles and the complexity of the reinforcement mechanism, it is relatively difficult to predict using conventional analytical and numerical models [54] [57] [58]. Ahmadian et al. [54] established a fast and reliable analytical model to predict the morphological changes of nanocomposite powders during mechanical alloying. There are also many differences in the influence of different particles on the material properties. Najjar et al. [57] found that the mechanical properties of the material were greatly improved due to the excellent mechanical properties of alumina, grain refinement, and dislocation motion impedance. Different processing methods also have an impact on the material properties [59-61]. The reinforcement of composite materials is caused by grain refinement, uniformity, reinforcing effect of particles, strain hardening, binding quality, and particle size [62, 63]. Meselhy et al. [64] derived the influence of the cumulative number of rolling runs on the tensile strength and elongation of metal matrix composite. It is found that tensile strength and elongation can be described as exponential functions of tract times. Elwan et al. [65]

investigated the effects of the addition of FeTiO_3 particles on the microtissue evolution and mechanical properties during the cumulative rolling of composites. The results showed that the dispersion of the particles improved with increasing rolling times.

A356 is a typical hypoeutectic Al-Si alloy composed of a-Al dendrites and eutectic Si. The flexibility of A356 is very low because the silicon phase is very brittle and unformable and cannot accommodate the plastic deformation of the surrounding matrix. The strength of A356 alloy is lower, because A356 alloy does not contain elements with obvious solid solution strengthening effects or can combine with the matrix to form intermetallic compound precipitation phases with high hardness, such as zinc and copper. To overcome the low strength problem, adding ceramic particles to A356 alloy to form the composite may be a feasible method [52, 53].

In this experiment, the mixed salt reaction method was used, and the $\text{A356-B}_2\text{O}_3\text{-KBF}_4$ reaction system was designed to prepare $(\text{AlB}_2 + \text{Al}_2\text{O}_3)/\text{A356}$ composites with mass fractions of 2 wt.%, 4 wt.%, 6 wt.%, and 8 wt.%, respectively. The morphology, distribution, and size of the generated AlB_2 and Al_2O_3 particles in situ were analyzed. The influence law of the particle content on the friction and wear behavior of the bipolar composite was studied to determine the optimal mass fraction. The mechanism of particles on friction reduction and wear resistance of composite materials is discussed.

2. Experimental Materials and Methods

2.1 Experimental Materials

The selected $(\text{Al}_2\text{O}_3 + \text{AlB}_2)$ duplex particle enhancement phase was used as the composite reinforcement of this experiment. The $\text{A356-B}_2\text{O}_3\text{-KBF}_4$ reaction system was used to prepare the $(\text{AlB}_2 + \text{Al}_2\text{O}_3)/\text{A356}$ composite material, and the in situ reaction equation is:



After calculation, the Gibbs free energy difference function (ΔG_{T}) can be expressed by

$\Delta G = \Delta H - T\Delta S = -385.11 < 0$ The calculation follows that the reaction can be performed spontaneously.

Raw materials explicitly used include:

1. B_2O_3 : Al_2O_3 particles were generated by reaction B_2O_3 with Al
2. KBF_4 : KBF_4 was reacted with Al to generate AlB_2 particles
3. Alloy A356 ingot: The main components of A356 alloy used in this experiment as the composite matrix were Si: 6.5 ~ 7.5, Mg: 0.3 ~ 0.45, Ti < 0.2, Fe < 0.12, Mn < 0.05, Cu < 0.1, Zn < 0.05, Al allowance (wt.%).

2.2 Experimental Methods

The preparation of $x\text{wt.}\% (\text{AlB}_2 + \text{Al}_2\text{O}_3)/\text{A356}$ ($x = 2, 4, 6, 8$) necessitates high-quality B_2O_3 and KBF_4 powders. The particle size of the ground powder mixture should be between 20 μm and 30 μm . To achieve this, two inorganic salt powders were dried at 250 °C for 2.5 hours, ground using a mortar, and mixed thoroughly. Next, the A356 alloy ingot was melted in a

Table 1 List of experimental raw materials

| Mass fraction | Al/g | KBF ₄ /g | B ₂ O ₃ /g |
|---------------|------|---------------------|----------------------------------|
| 2 wt.% | 1000 | 51.4 | 14.3 |
| 4 wt.% | 1000 | 102.8 | 28.6 |
| 6 wt.% | 1000 | 154.2 | 42.9 |
| 8 wt.% | 1000 | 205.6 | 57.2 |

high-frequency induction furnace and superheated to 850 °C in air. The mixed salt was poured into the molten aluminum liquid using a graphite bell cover and stirred well. After 30 min of reaction time, a refining agent (1 wt.% C₂Cl₆) was added to the melt to refine it, followed by the addition of a slag removal agent. The melt was then allowed to cool down to 720 °C before being cast into an iron mold measuring 200 mm × 100 mm × 20 mm. Table 1 shows the raw materials used.

A quantitative analysis was conducted on the microstructure, material composition, and grain size of the composites. Additionally, the elements present in the material were qualitatively analyzed using the EDS energy spectrum. The 3D confocal microscope was utilized to measure the average cross-sectional area of the ground mark, and the wear rate of the sample was calculated via a formula. To prepare the friction wear test sample, wire cutting was implemented to create a 15 mm * 15 mm * 3 mm sample. Subsequently, the treated friction wear test sample was subjected to the HT-1000 high-temperature friction wear test machine at room temperature. Table 2 displays the specific parameters employed during the friction and wear test. Finally, three trial material tests were performed to obtain the average of the final results.

3. Effects of Particle Content on Micro-Organization and Friction Wear Behavior

3.1 Phase and Microtissue Analysis

3.1.1 Phase-Wise and Polarimetric Analysis. X-ray diffraction (XRD) analysis was conducted on both A356 aluminum alloy and four groups of (AlB₂ + Al₂O₃)/A356 composites with varying enhanced particle mass fractions. Figure 1 presents the diffraction curves obtained during the analysis. The black line in the figure represents the diffraction curve of the A356 aluminum alloy, which primarily comprises five prominent peaks of Al and some Si phases. Additionally, weak peaks were observed alongside the dominant diffraction peaks of primary aluminum. Subsequent analysis revealed that these weak peaks corresponded to the Al₂O₃ and AlB₂ phases, respectively. Therefore, it can be concluded that the composite material successfully incorporated target-enhanced AlB₂ and Al₂O₃ particles. Notably, the strength of the weak peaks increased with increasing mass fraction, indicating a higher content of corresponding phases in the composite material. These results prove that the prepared composite materials' enhanced particle mass fraction aligns with the designed gradient increment.

The photomicrographs depict grains in various position directions, which appear in different colors. The dark regions, both large and small, may indicate clusters of particles in the composite material or defects such as stomata that occurred

Table 2 Room temperature friction and wear test parameters (The experiment time was 20 min and the friction radius was 4 mm)

| Speed/rpm | Loading/N |
|-----------|-----------|
| 200 | 5 |
| 200 | 10 |
| 200 | 15 |
| 250 | 10 |
| 300 | 10 |

during material preparation. Figure 2 shows that the black areas are present regardless of whether the enhanced particle mass fraction is 2 wt.% or 8 wt.% (AlB₂ + Al₂O₃)/A356 composite. Most of the black region is located at the crystal boundary with only a minimal amount within the crystal. Moreover, the significant number of large black areas in the 8 wt.% composite material is due to an increase in the number of enhanced particles resulting in particle agglomeration to reduce interface energy. To achieve even distribution and minimize accumulation, the composite is synthesized using strengthening mixing or other methods of mixing.

Polarized photographs of the composite were analyzed, and the grain size was calculated. The A356 matrix, 2 wt.%, 4 wt.%, 6 wt.%, and 8 wt.% (AlB₂ + Al₂O₃)/A356 composite were approximately 266.1 μm, 205.5 μm, 175.1 μm, 158.6 μm, and 163.1 μm, respectively. And the distribution of the grain size is shown in Fig. 3.

3.1.2 Microhardness analysis. Figure 4 is a microhardness diagram of the A356 alloy and an enhanced A356 composite with different duplex particle content. As can be seen from the figure, the Vicker microhardness change trend of the A356 matrix and the composite material is inversely proportional to the α-Al grain size in the material. This phenomenon is consistent with the Hall–Petch formula at the micron scale, representing more grain boundaries per unit area of such matrix grains refined by enhanced grains. The shear deformation of adjacent grains must produce sufficient stress concentration at the grain boundary. Refinement grains create more grain boundaries. If the crystal boundary structure does not change, a more significant external force is needed to generate a dislocation blockage and strengthen the material.

3.1.3 OM Analysis. As can be seen from Fig. 5, the composite after the keller reagent corrosion crystal boundary under the light mirror, and can clearly see many black and white layer sheet or needle distribution at the boundary, this is A356, alloy Si phase, presents a black and white needle, because Si and Al formed Al-Si common crystal tissue. Figure 5 can also observe many near yellow bars or short rod particles, and the near yellow particles are AlB₂ particles. Due to the phase analysis of the particles, the light microscope will conduct qualitative phase analysis by scanning electron microscope to prove that the particles are AlB₂ particles. However, it is difficult to observe the Al₂O₃ particles of the composite in Fig. 5, because the size of Al₂O₃ particles is generally in nanometers or several micrometers, so it is difficult to find under the light mirror, or some similar particles can be found but their composition cannot be confirmed. In addition, there are also in Fig. 5 a little dark black round spots, according to the literature reading and combined with the spot size, think

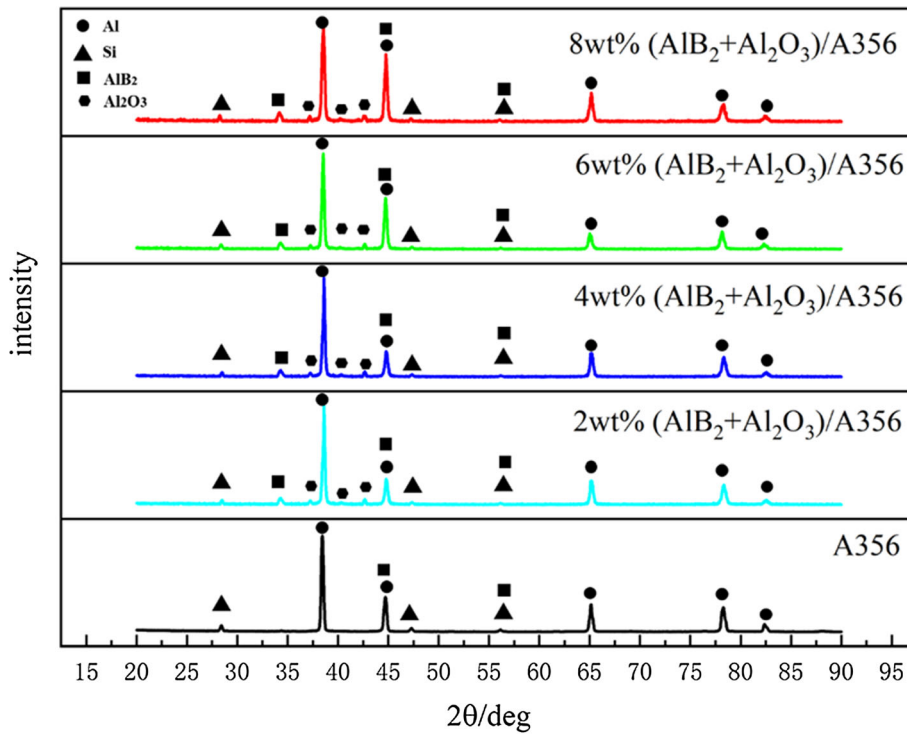


Fig. 1 XRD patterns of A356 alloy and (AlB₂ + Al₂O₃)/A356 composites with different particle contents

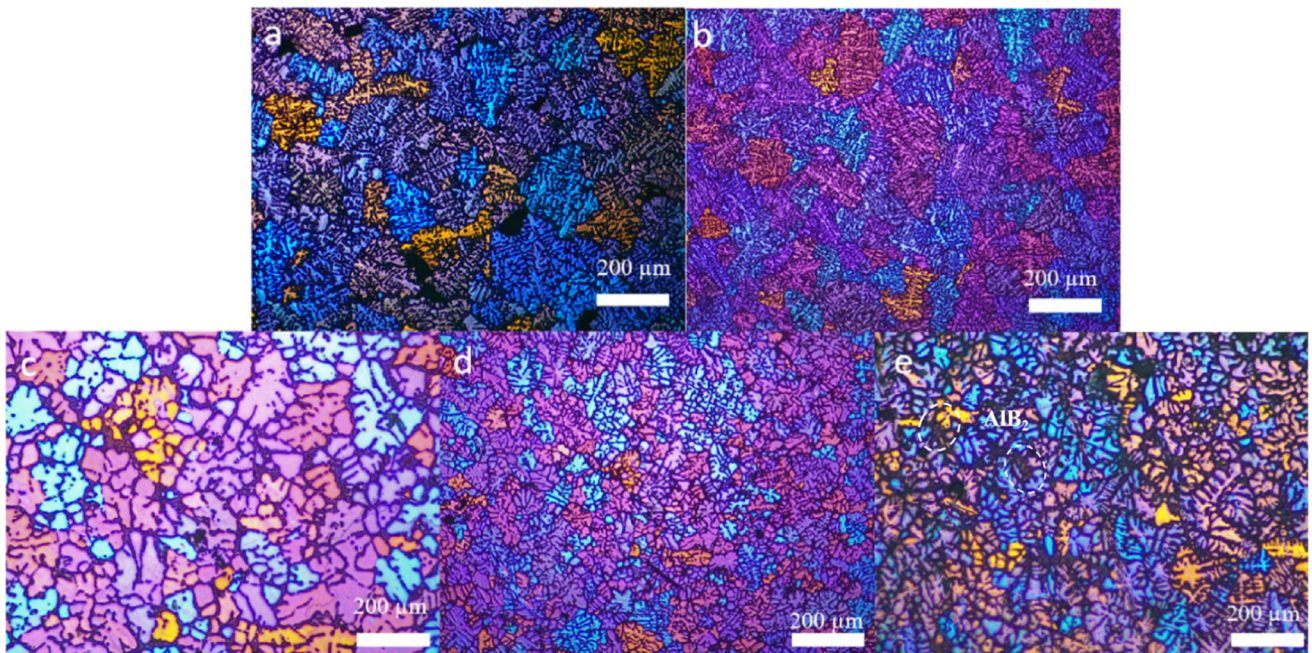


Fig. 2 Polarized light micrographs of (AlB₂ + Al₂O₃)/A356 composites with different particle contents. (a) A356; (b) 2 wt.%; (c) 4 wt.%; (d) 6 wt.%; (e) 8 wt.%

these dark black spots may be stomatal defects, because the system reaction will produce KAlF₄ gas, and the experimental process after the material reaction step is not careful, triad refining agent after joining the stirring degree and retention time is insufficient; there is a little pore during casting.

Figure 5(a), (b), (c), and (d) is 200 times the metallographic point; obviously, from (a) to (d), the number of AlB₂ particles

gradually increases; in addition, from Fig. 5(a), (b), (c), and (d) we can see AlB₂ particles more distributed at the grain boundary and more particle agglomeration, and this may be because the material crystallization, AlB₂ particles by the matrix aluminum crystal boundary, when more AlB₂ particles are pushed to the boundary, to reduce the surface energy to

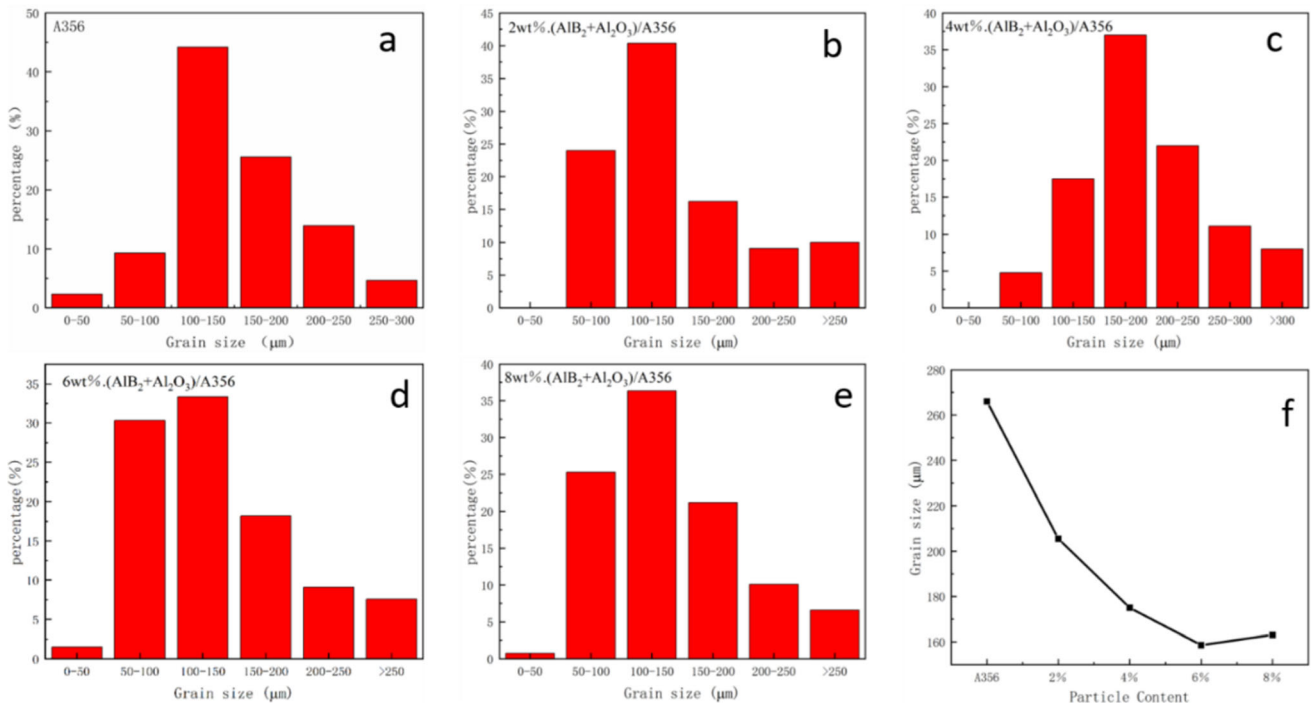


Fig. 3 Grain size distribution of different composites and A356 alloy. (a) A356, (b) 2 wt.%, (c) 4 wt.%, (d) 6 wt.%, (e) 8 wt.%, (f) the distribution of the grain size

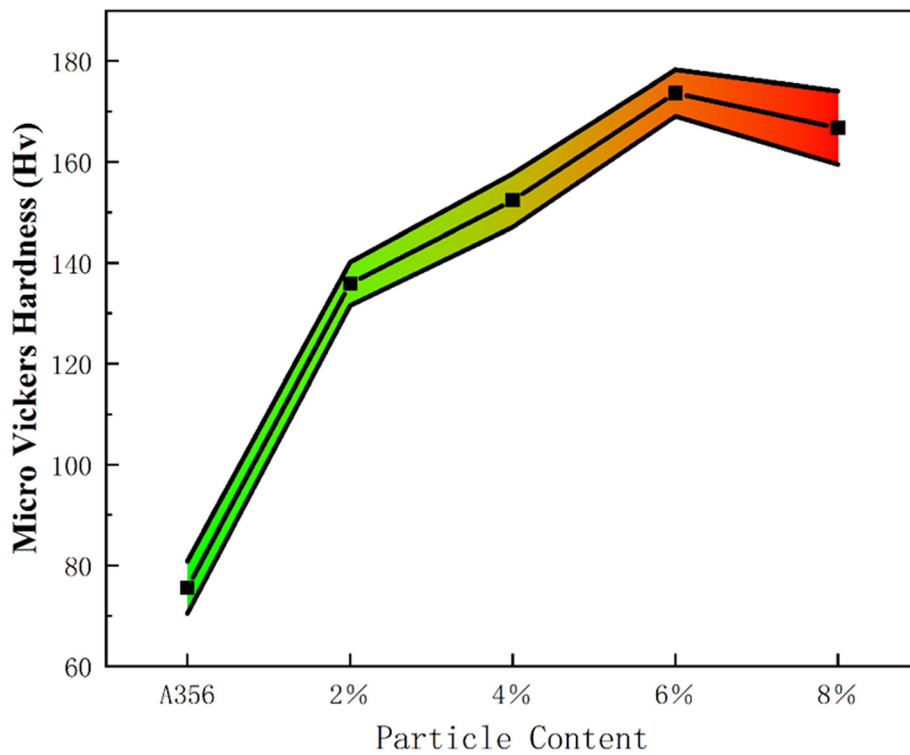


Fig. 4 The Micro Vickers Hardness of the matrix and A356 composites reinforced with different content of dual-phase particles

reduce the overall energy to the system to achieve stable state, and AlB_2 particles agglomeration phenomenon.

3.1.4 SEM and Energy Spectrum Analysis. From Fig. 6, we can see many small silver-gray or even black square or long rod-shaped particles. Through the EDS spectral

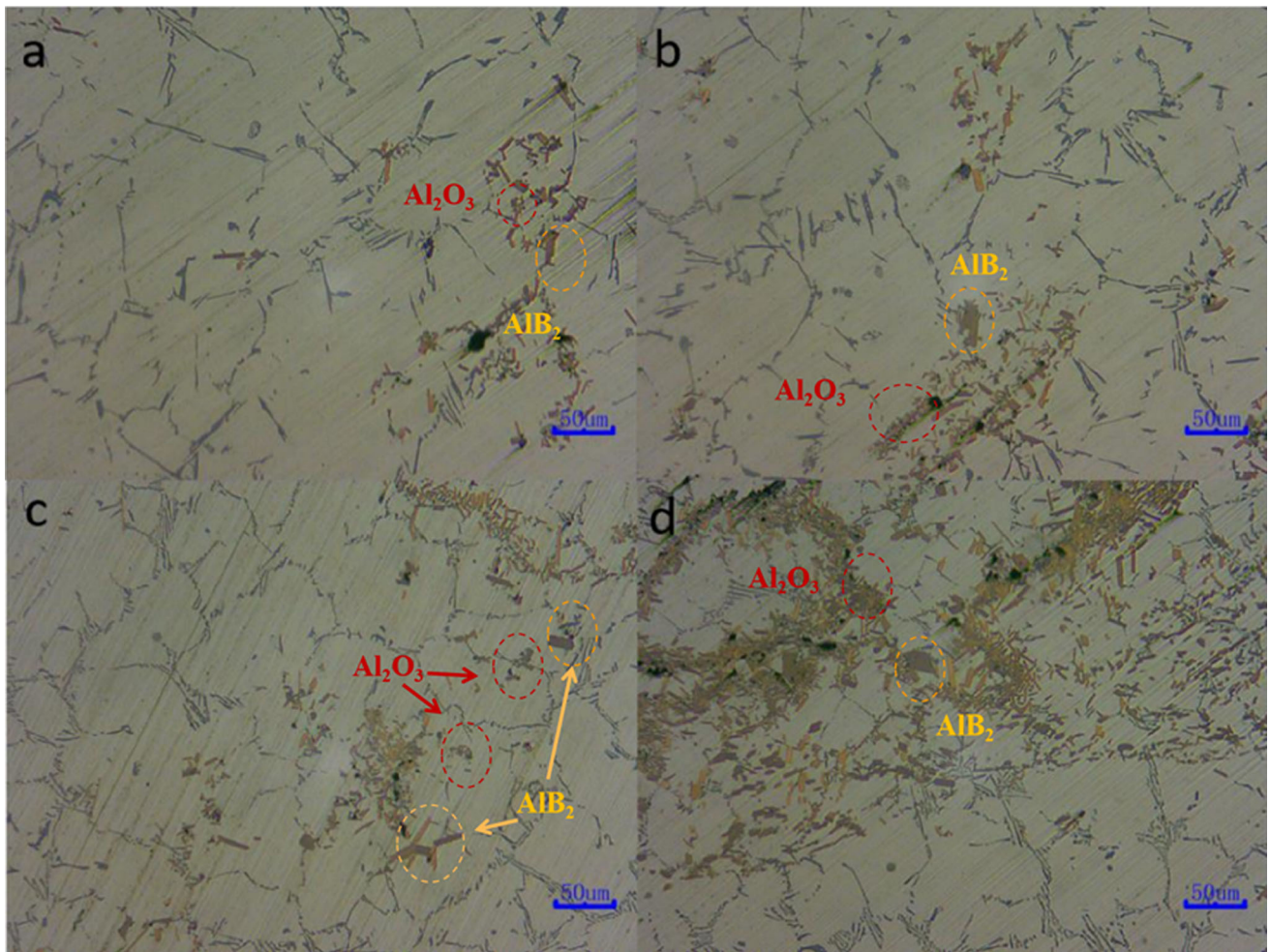


Fig. 5 Metallographic micrographs of (AlB₂ + Al₂O₃)/A356 composites. (a) 2 wt.%; (b) 4 wt.%; (c) 6 wt.%; (d) 8 wt.%

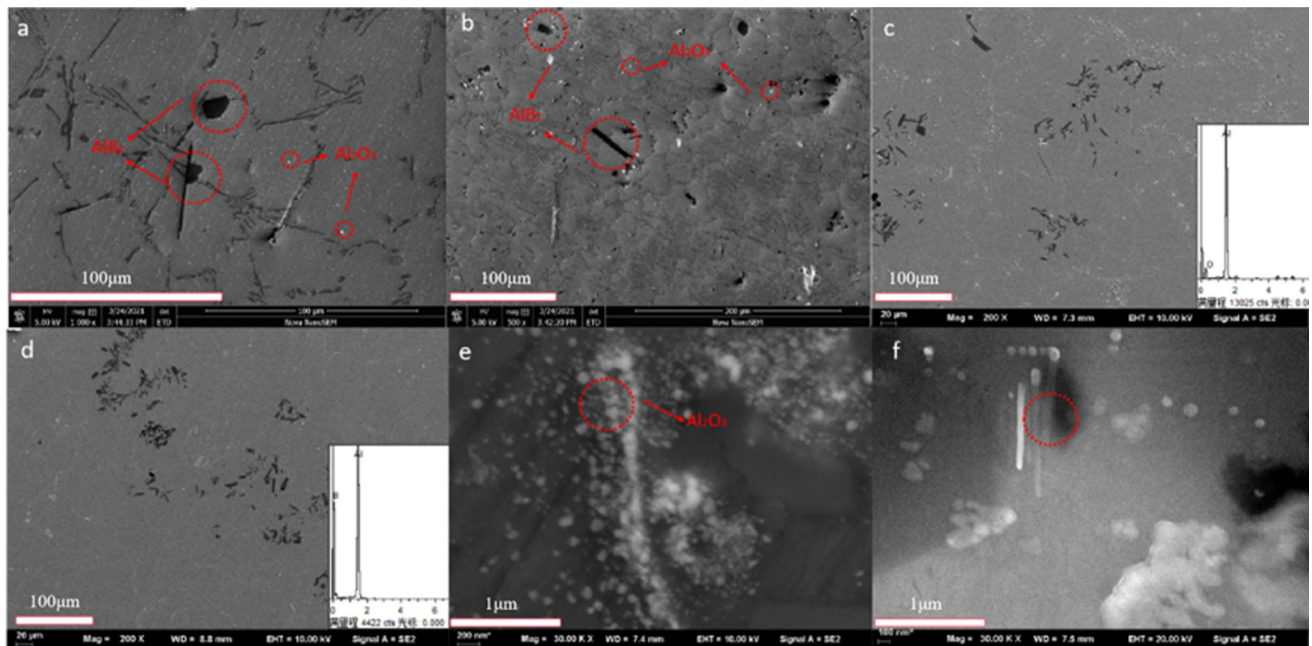


Fig. 6 SEM of (AlB₂ + Al₂O₃)/A356 composites. (a) 2 wt.%; (b) 4 wt.%; (c) 6 wt.%; (d) 8 wt.%

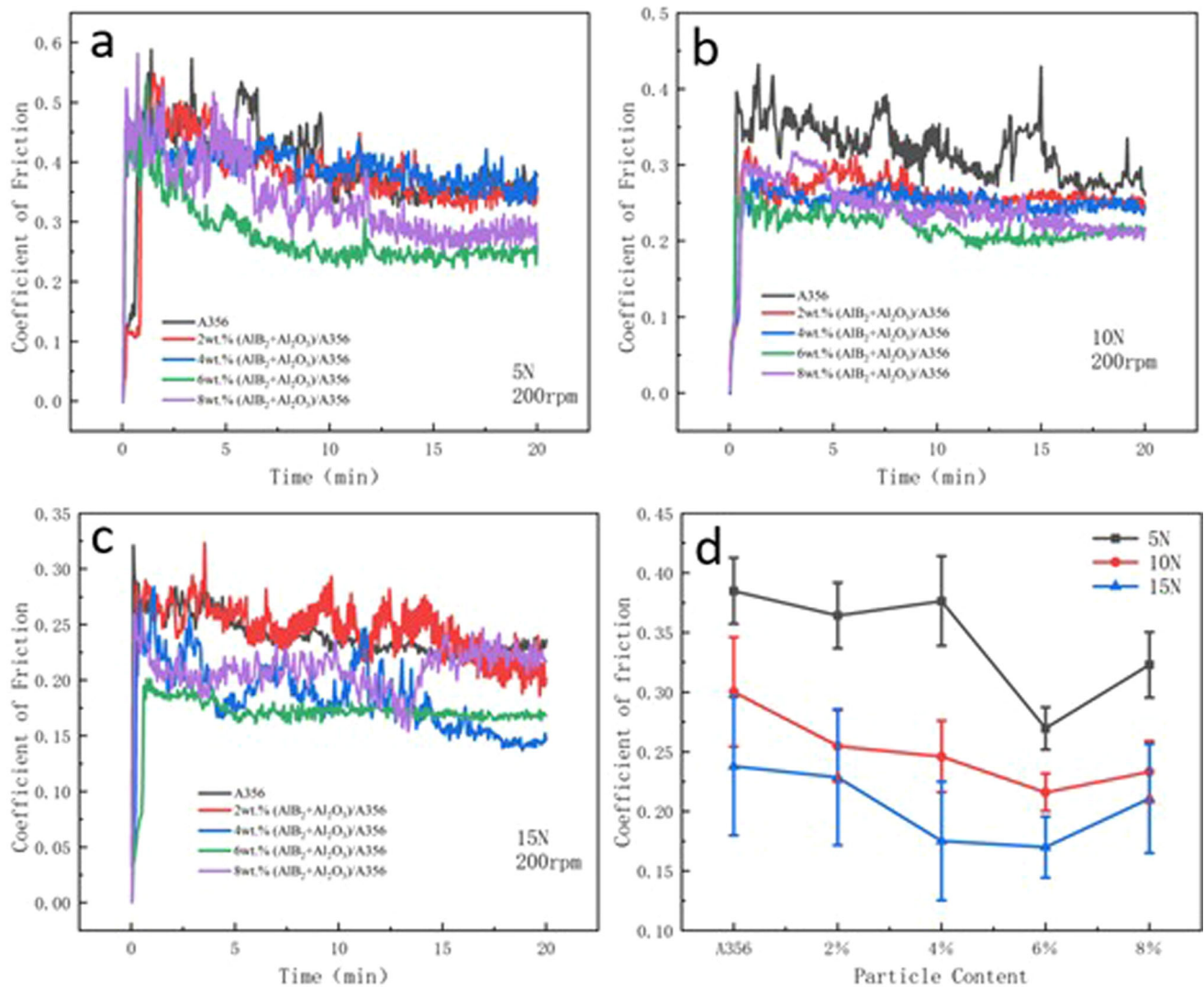


Fig. 7 Coefficient of friction of A356 matrix and xwt.% (AlB₂ + Al₂O₃)/A356 composite under different loads. (a) 5N 200 rpm; (b) 10N 200 rpm; (c) 15N 200 rpm; (d) average friction coefficient

detection results (Fig. 6d), these long rods or massive objects are AlB₂ particles with a radial size of about 11 μm. In addition, the presence of a large number of bright white dots or small sheet particles of the material is also clearly visible. These bright white particles were analyzed as Al₂O₃ particles by EDS results (Fig. 6c).

As can be seen from the figure, with the improvement of the enhanced particle mass fraction, random sampling of rod particles and bright white dot particles quantity increased, and the number of particles increased significantly, the effect is noticeable, which further proves that the system can control the reaction of raw material salt by calculation and then control the enhanced particle mass fraction. It is evident from Fig. 6(a), (b), (c), and (d) that the Al layer particles of rod-shaped AlB₂ are distributed at the crystal boundary and have different orientations because the crystal structure of AlB₂ is a graphite-like sheet structure of Al and B atoms alternately arranged. The Al atomic layer is easy to converge to the Al layer of the Al-Mg₂Si sheet co-crystal phase along the crystal boundary, thus

minimizing the interface energy to achieve the most stable state. Therefore, the AlB₂ particles have different orientations from the precipitation phase orientation. From Fig. 6(a), (b), (c), and (d), we can also observe a large number of fine bright white alumina particles. Compared with AlB₂ particles, the alumina particles are more evenly distributed and slightly scattered, but there are inevitably many polarization areas, and the Al₂O₃ particles are mostly clustered into strips or sheets.

As can be seen from Fig. 3, AlB₂ particles are primarily black and short rod shaped, while Al₂O₃ particles have a large number of small-size round particles, while many long, rod-shaped, and massive Al₂O₃ also appear. As shown in the red box mark in Fig. 6(e), several circular Al₂O₃ particles can be found in the nanometer range at 30 K x shooting. Moreover, marked by the red circle shown in Fig. 6(f), the block Al₂O₃ and the sheet AlB₂ particles are accompanied, and it is evident that the interface between the two particles is purely and tightly bound.

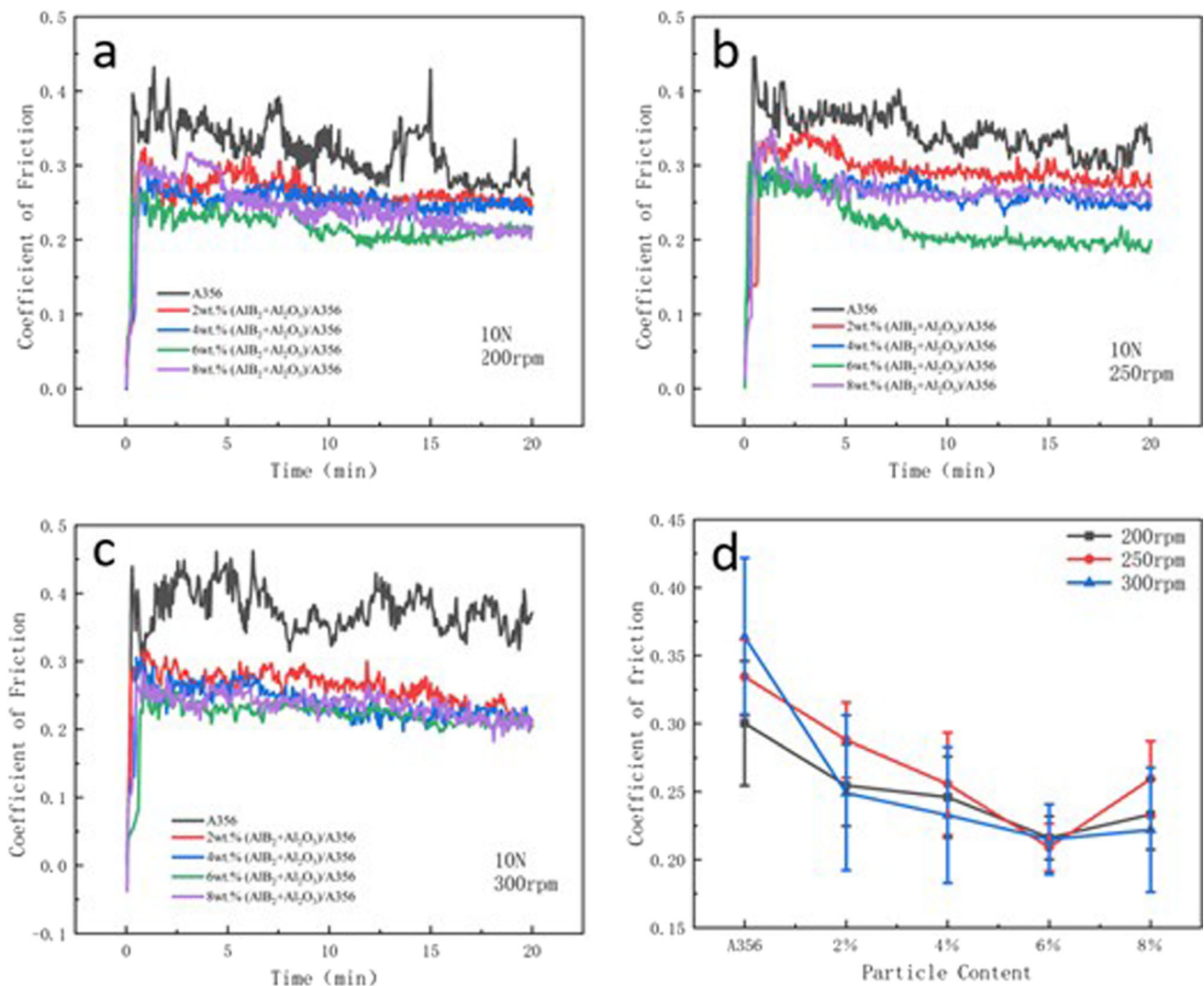


Fig. 8 Coefficient of friction of A356 matrix and xwt.% (AlB₂ + Al₂O₃)/A356 composite under different rotating speed. (a) 10N 200 rpm; (b) 10N 250 rpm; (c) 10N 300 rpm; (d) average friction coefficient

3.2 Study on Friction and Wear Behavior

3.2.1 The Influence of the Load and Rotational Speed on the Coefficient of Friction. Figure 7 and 8 show that the addition of AlB₂ particles and Al₂O₃ particles has some friction reduction effect on the material. This is because the AlB₂ particles and the Al₂O₃ particles act as buffer layers in the A356 matrix alloy. At different loads and different speeds, the mass fraction of the Biphasic particles increased from 2% to 8%. The friction coefficient of the composite material decreased by an average of 8.1%, 15.6%, 28.8%, 16.6% (load), 20.2%, 25.9%, 35.5%, and 27.9% compared with the A356 alloy matrix (rotation speed). This indicates that the content of the biphasic particles and their dispersion on the composite surface can significantly affect the friction coefficient of the material in the friction tests. The increasing bipolar particle content tends to reunite, and the agglomeration of duplex particles leads to a relatively rough composite surface, which is the best effect when the bipolar particle mass fraction reaches 6 wt.%. As seen in Fig. 7, the friction coefficient of the material decreases as the

load increases. We believe that the friction wears mechanism changes from adhesive wear to grinding grain abrasion, thus reducing the friction strength and friction coefficient. As seen in Fig. 8, the friction coefficient curve becomes relatively unstable with the increase in the rotation speed because the high rotation speed increases the friction surface temperature and changes the friction wear mechanism to oxidative wear, and excessive oxides on the friction surface lead to increased roughness.

3.2.2 Effect of the Load and Rotational Speed on the Wear Resistance. Figure 9 and 10 show that the amount of wear on all materials increases to some extent as the load increases. Under the same load, the composite with added (AlB₂ + Al₂O₃) particles has less wear and wear rates than the A356 alloy. This indicates that the addition of (AlB₂ + Al₂O₃) particles significantly improves the wear resistance of the material. Under the same load, when the particle content is 6 wt.%, the wear rate of the composite is reduced by 43.5% (5N), 451.1% (10N), and 59.8% (15N) than the A356 alloy,

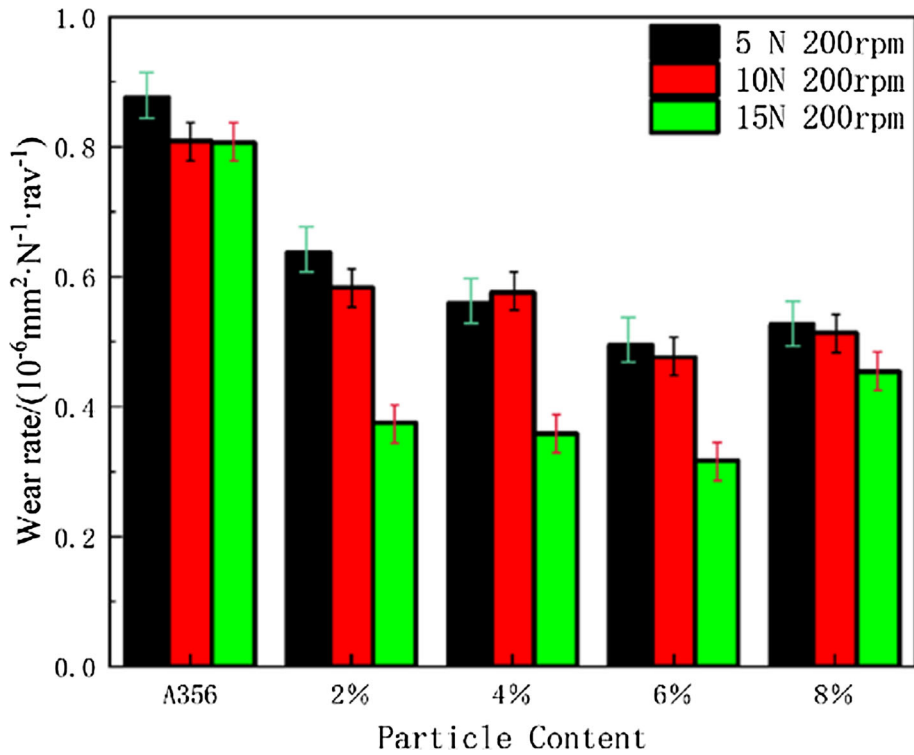


Fig. 9 Wear rate of A356 matrix and xwt.%(AlB₂ + Al₂O₃)/A356 composite under different loads

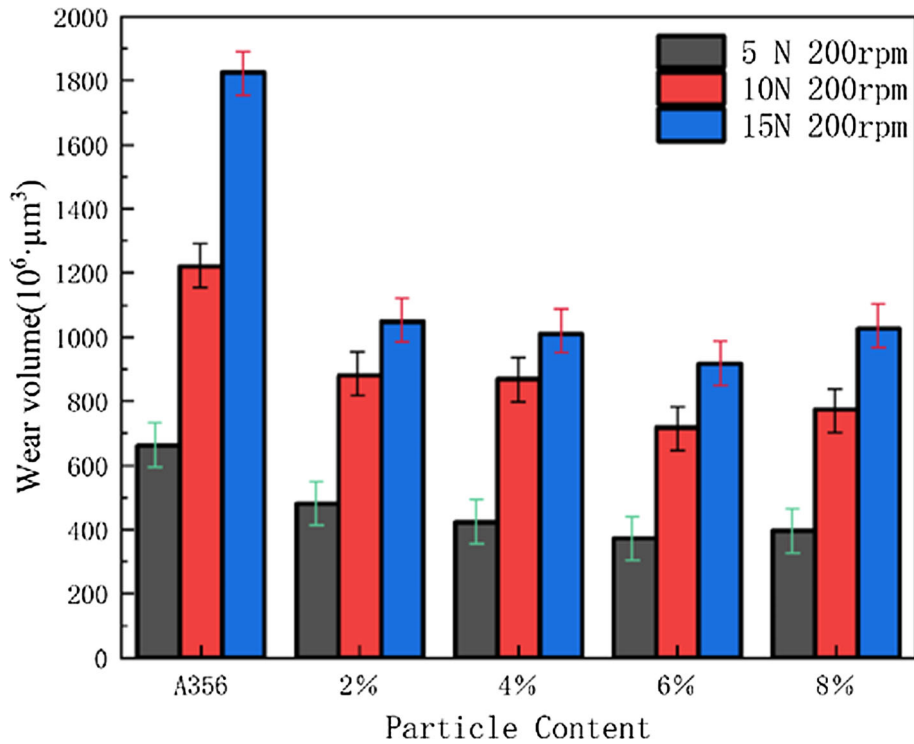


Fig. 10 Wear volume of A356 matrix and xwt.%(AlB₂ + Al₂O₃)/A356 composite under different loads

respectively. From Fig. 10, almost all materials decrease as the load increases. There are two reasons for this: One is the change of wear mechanism, from sticky wear to abrasive wear, thus reducing the wear strength. On the other hand, during the wear

process, the adhesive wear-peeling material is welded to the material surface, and the wear rate is reduced. The first reason is that it is more conducive to the wear resistance of the material.

From Fig. 11(a), (b), and (c), there is a sizeable peeling layer. This is because with the increased load, the A356 alloy

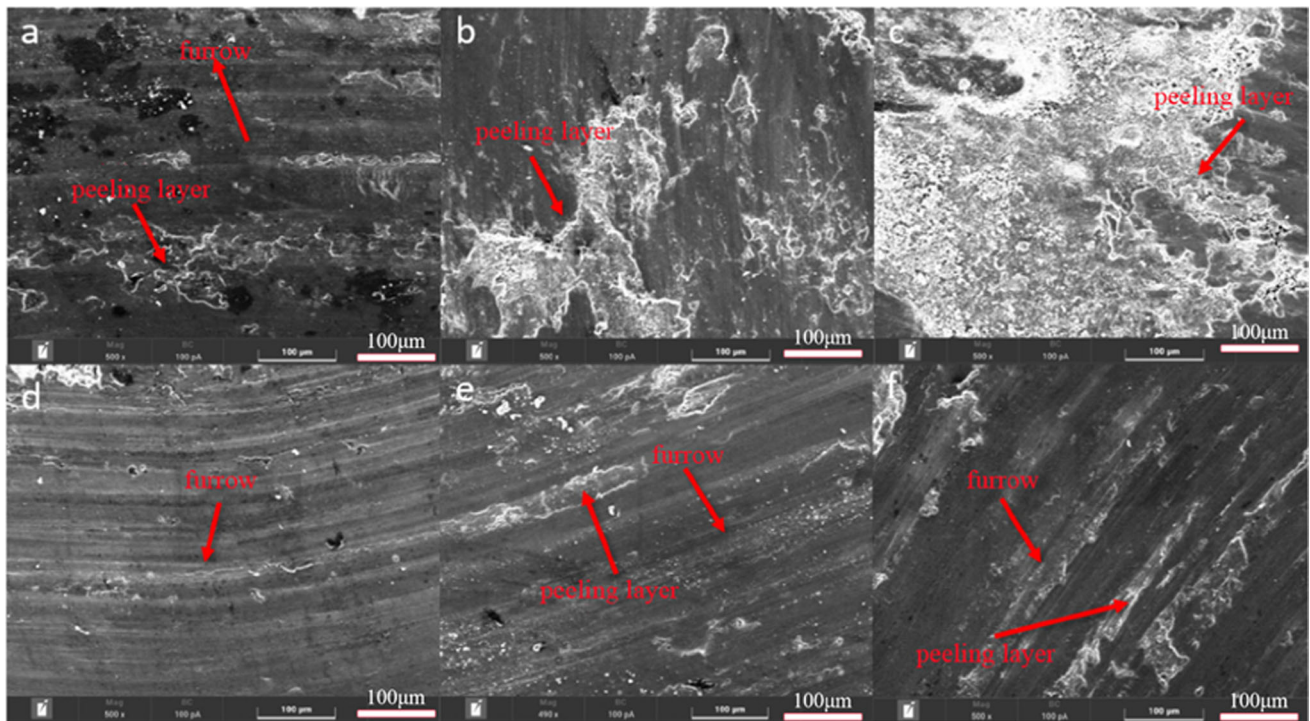


Fig. 11 SEM images of wear morphologies of A356 alloy and 6 wt.% (AlB₂ + Al₂O₃)/A356 composite under different loads (a-c) A356; (d-f) 6 wt.% (AlB₂ + Al₂O₃)/A356; (a, d) 5N; (b, e) 10N; (c, f) 15N

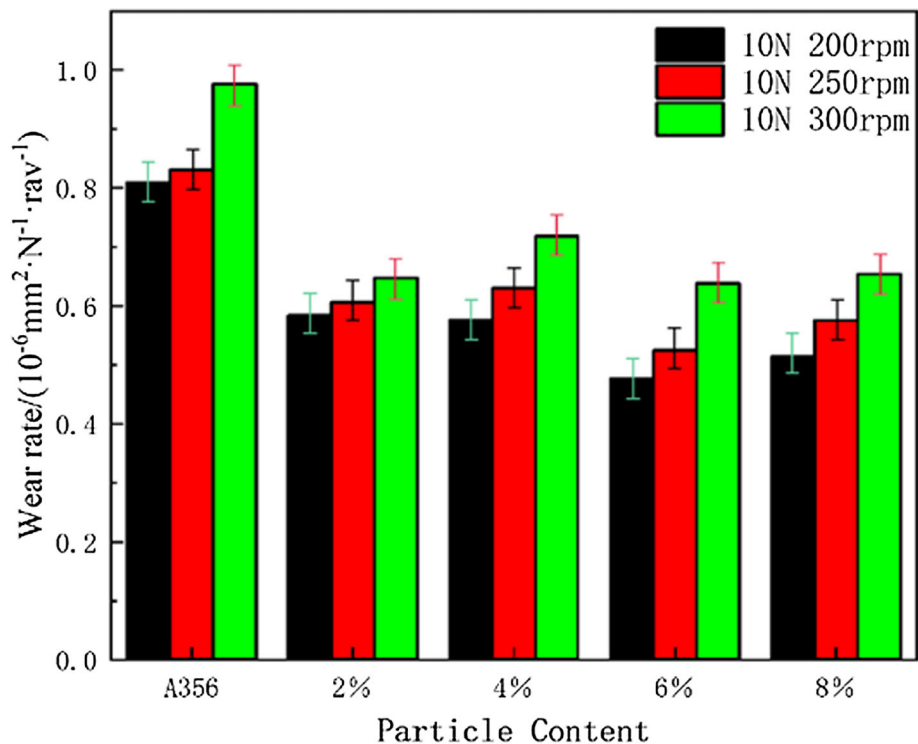


Fig. 12 Wear rate of A356 matrix and xwt.%(AlB₂ + Al₂O₃)/A356 composite under different rotating speed

subsurface crack also increases, resulting in massive peeling, and the primary wear mechanism is adhesive wear. In Fig. 11(d), (e), and (f), the wear surface of the 6 wt.% (AlB₂ + Al₂O₃)/A356 composite is flatter than the wear surface of the A356 alloy. The precise groove and fine peeling layer

indicate that the wear mechanism is mainly abrasive wear and slight adhesive wear.

Figure 12 and 13 show the amount and rate of wear at different rotational speeds. As with the wear under other loads, the amount of wear of the same material increases with the

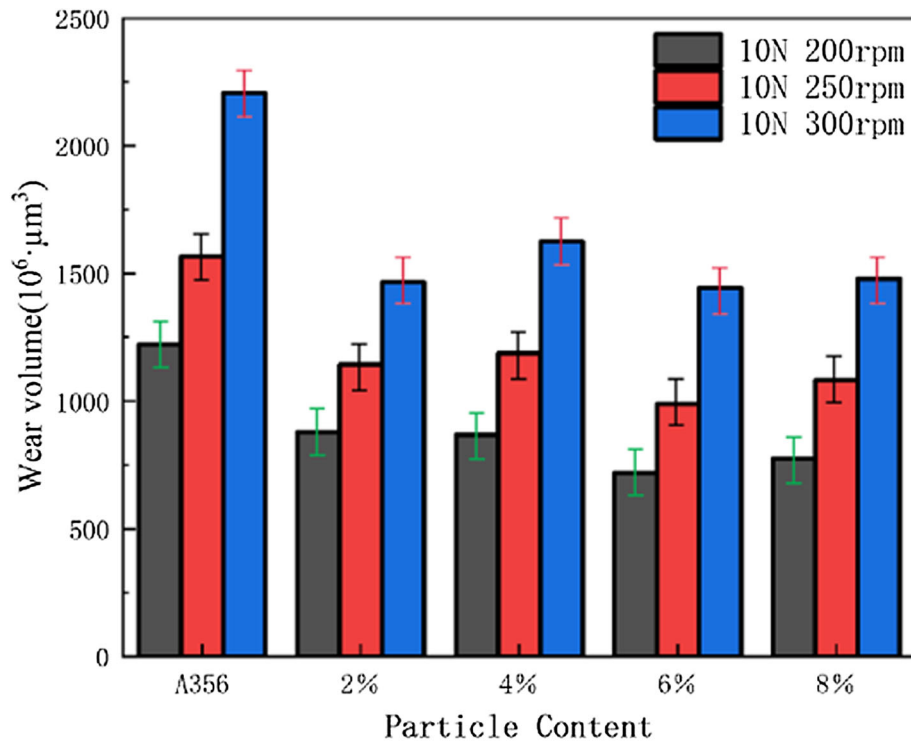


Fig. 13 Wear volume of A356 matrix and xwt.%(AlB₂ + Al₂O₃)/A356 composite under different rotating speed

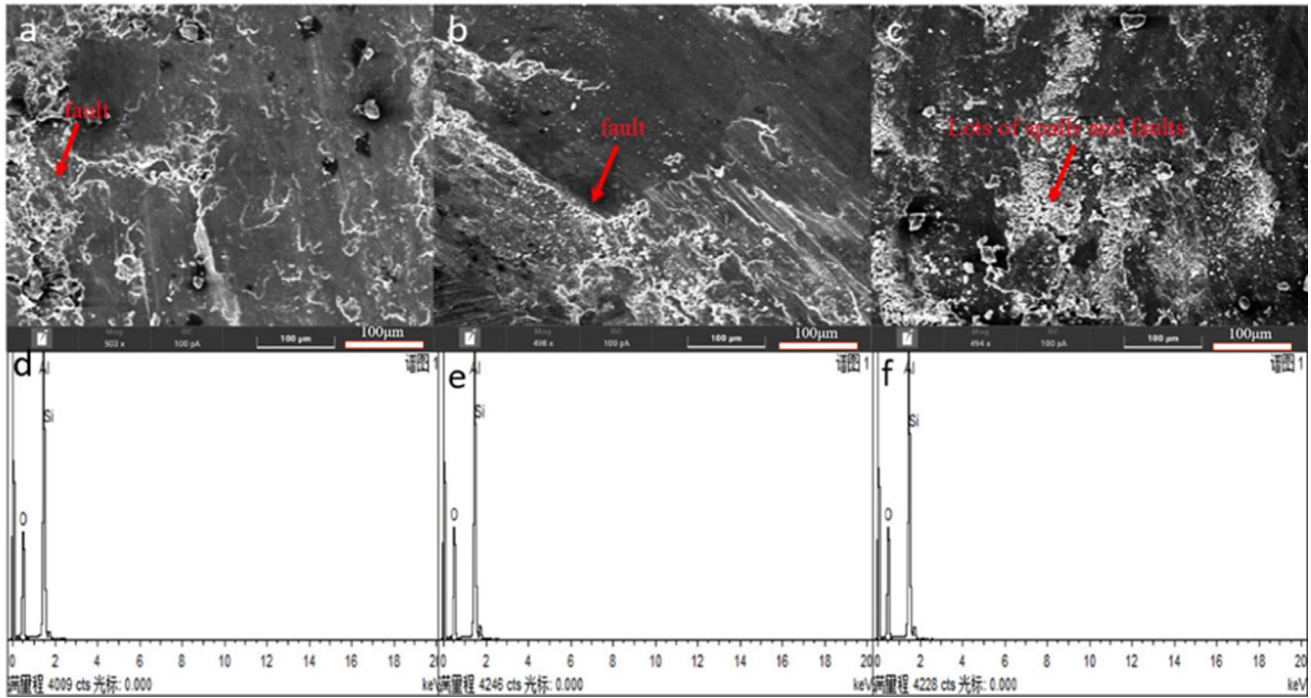


Fig. 14 SEM images of wear morphologies of A356 alloy composite under different rotating speed. (a) 200 rpm; (b) 250 rpm; (c) 300 rpm; (d-f) EDS mapping

rotation speed, while the composite material is less worn than the A356 alloy. Unlike wear at different loads, the wear rate of almost all materials increases with increasing speed. Under different loads or different speeds, the addition of biphasic particles is conducive to improving the wear resistance of the material. When the bipolar particle mass fraction reaches

6 wt.%, the wear rate of the composite is the most reduced compared with the A356 alloy, reaching 41.1% (200 rpm), 36.9% (250 rpm), and 34.6% (300 rpm), respectively.

From Fig 14(a), (b), and (c), there are severe subsurface fractures of the A356 alloy and obvious oxides. Using the EDS energy spectrum of the wear surface, it is not difficult to see that the

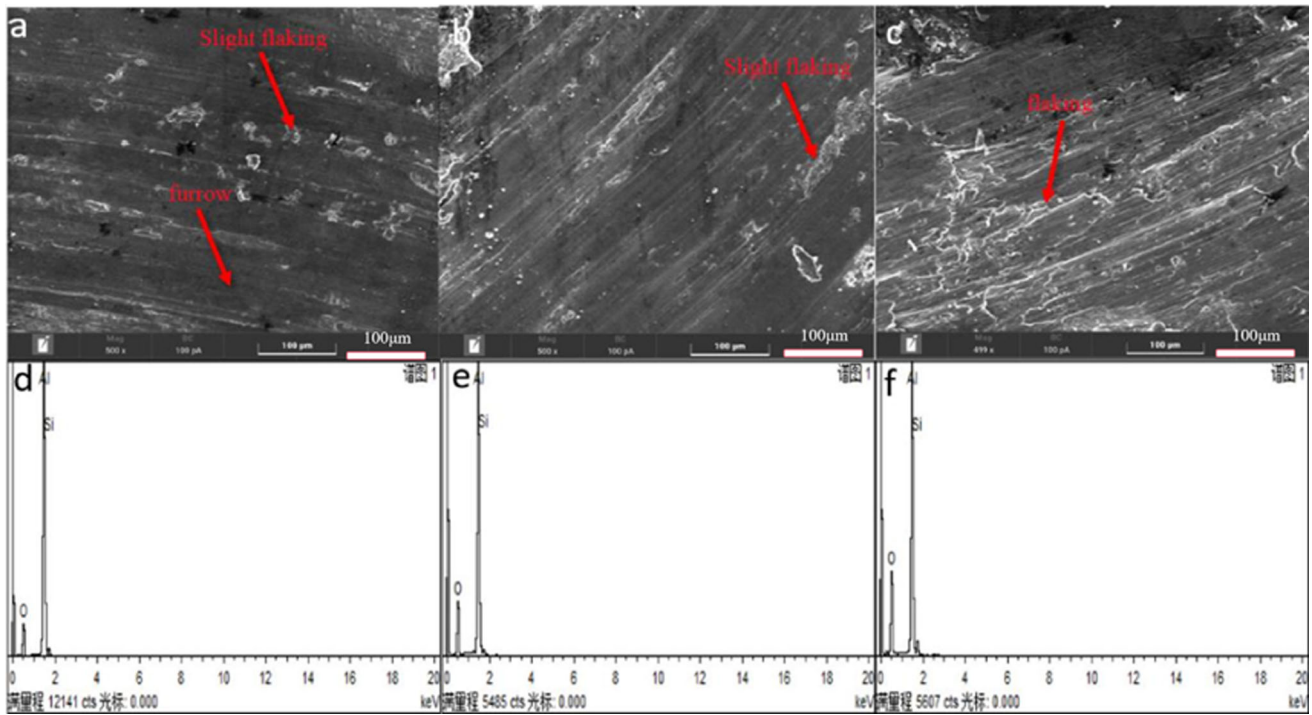


Fig. 15 SEM images of wear morphologies of 6 wt.%(AlB₂ + Al₂O₃)/A356 composite under different rotating speed. (a) 200 rpm; (b) 250 rpm; (c) 300 rpm; (d-f) EDS mapping

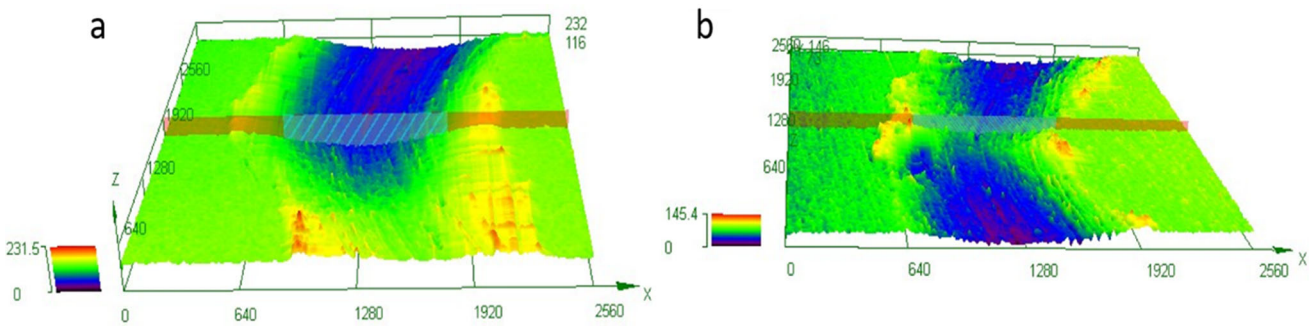


Fig. 16 3D confocal images of wear scar morphology of different materials; (a) A356; (b) 6 wt.%(AlB₂ + Al₂O₃)/A356 composite; load: 15N. Rotating speed: 200 rpm

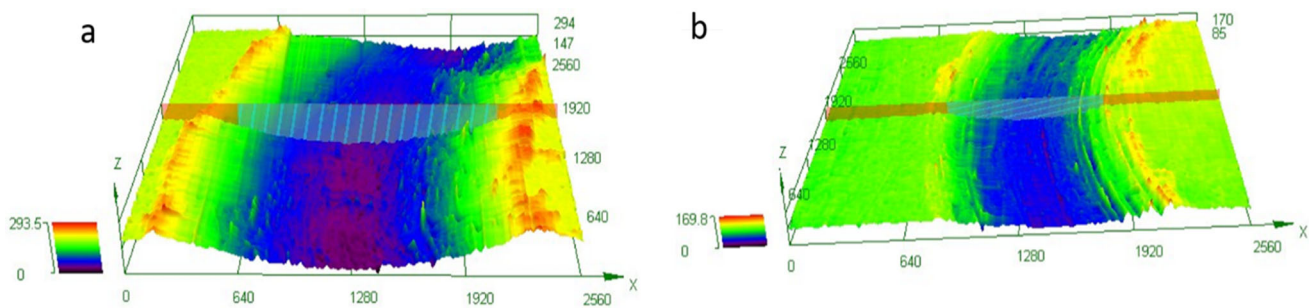


Fig. 17 3D confocal images of wear scar morphology of different materials; (a) A356; (b) 6 wt.%(AlB₂ + Al₂O₃)/A356 composite; load: 10N. Rotating speed: 300 rpm

oxygen content represented by the wear increases with increasing speed. When the speed increases by 300 rpm, the main mechanism of A356 alloy wear is oxidative wear. This is due to the large amount of friction heat generated at high speed, making the A356

alloy more easily oxidized. In Fig. 15(a), (b), and (c), it is clear that 6 wt% (AlB₂ + Al₂O₃)/A356 composite wear did not exhibit a subsurface fracture. Some oxides and grooves indicate that the wear mechanism is oxidative wear and grinding abrasion. The

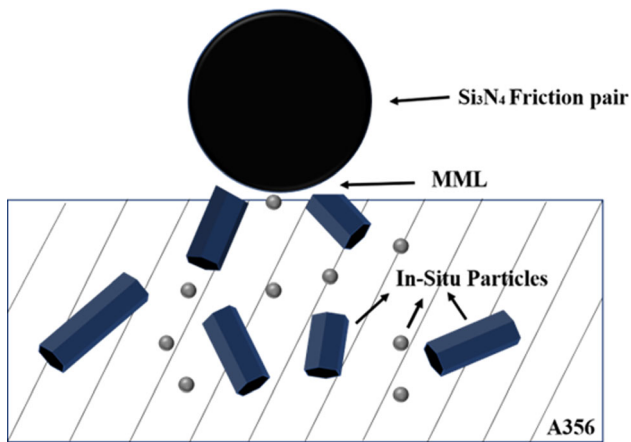


Fig. 18 Tribological behavior model diagram of composites

EDS energy spectrum shows that the oxygen content of the wear surface is not as high as that of the A356 alloy. This is because: (1) $(\text{AlB}_2 + \text{Al}_2\text{O}_3)$ refines the grain of the matrix, increasing the hardness of the material and hindering the fracture of the material surface during the wear process, and (2) $(\text{AlB}_2 + \text{Al}_2\text{O}_3)$ particles can act as a buffer layer on the material surface so that the friction strength of the wear surface is lower than the A356 alloy.

As shown in Fig. 16, under the conditions of 15N, 200 rpm, the abrasion depth of the material was reduced from 231.5 μm of the A356 matrix to 145.4 μm of the composite material, decreasing by 37.19%. Figure 17 shows that the wear depth at 10N, 300 rpm of the material decreased from 293.5 μm for the A356 matrix to 169.8 μm for the composite by 42.14%. It can be seen that the friction and wear behavior of the composite material under the influence of load or speed is greatly improved compared with the A356 matrix.

3.3 Analysis of Friction and Wear Mechanism at Room Temperature

The paper presents the friction wear model of composites, illustrated in Fig. 18. The wear surface forms a mechanical mixing layer (MML), which improves the material's friction properties by creating a thin layer of MML. This effect is achieved by AlB_2 and Al_2O_3 particles mixed into the composite. The presence of AlB_2 and Al_2O_3 particles reduces the friction contact surface and creates a microbulge in the MML, leading to a reduced and stabilized friction coefficient. This observation is consistent with the earlier analysis of the change in friction coefficient. These results confirm that the addition of AlB_2 and Al_2O_3 particles optimizes the friction and wear behavior of A356 alloy. Additionally, these particles act as Orowan strengthening agents and refine the tissue, thereby increasing the material's crystal boundary and resistance to displacement. Refining the particles also increases the number of grains and movable sliding systems, resulting in a more uniform distribution during wear and improved wear resistance.

4. Conclusion

In this study, we designed a reaction system consisting of A356, B_2O_3 , and KBF_4 . The aim was to synthesize dual-phase particle-reinforced aluminum matrix composites with anti-

friction and wear-resistant properties through an in situ mechanical stirring mixed salt reaction method. We conducted investigations on the changes in microstructure and morphology as well as the friction and wear properties at room temperature. Based on our findings, we draw the following conclusions:

- Through XRD analysis, AlB_2 and Al_2O_3 duplex-enhanced particles were successfully prepared in the A356- B_2O_3 - KBF_4 reaction system. Through metallographic analysis ($\text{AlB}_2 + \text{Al}_2\text{O}_3$)/A356 composite material, it was found that the morphology of AlB_2 enhanced particles were mostly short rods and distributed by local clusters.
- Microscopy, the A356 aluminum alloy and the $(\text{AlB}_2 + \text{Al}_2\text{O}_3)$ /A356 composite-Al grain size with mass fractions of 2 wt.%, 4 wt.%, 6 wt.%, and 8 wt.% were calculated, and the results were 266.075 μm , 205.5 μm , 175.1 μm , 158.6 μm , and 163.1 μm , respectively. The best effect on-Al grain refinement was achieved when the duplex particle mass fraction reached 6 wt.%.
- The analysis of SEM and EDS data of $(\text{AlB}_2 + \text{Al}_2\text{O}_3)$ /A356 composite found that AlB_2 particles are mostly micron size and Al_2O_3 particles are mostly nanosize. Both enhanced particles reunite. AlB_2 particles and Al_2O_3 particles can grow with each other, and the interface is very close.
- To study the friction and wear behavior of the $(\text{AlB}_2 + \text{Al}_2\text{O}_3)$ /A356 composite materials with the A356 alloy and the particle mass fractions of 2 wt.%, 4 wt.%, 6 wt.%, and 8 wt.%, respectively, when the mass fraction of the biphasic particles is 6 wt.%, $(\text{AlB}_2 + \text{Al}_2\text{O}_3)$ /A356 composite material has the best friction reduction effect and wear resistance over the A356 matrix alloy matrix. The wear mechanism of 6 wt.% $(\text{AlB}_2 + \text{Al}_2\text{O}_3)$ /A356 composite is mainly abrasive wear. The wear mechanism of A356 matrix alloy is mostly adhesive wear.

Acknowledgments

This work is financially supported by the National Natural Science Foundation of China, Nos. 52071158, U20A20274, U1664254. High end Foreign Experts Introduction Program of the Ministry of Science and Technology of China G2022014134L, G2022014043.

Conflict of interest

All authors certify that they have no affiliations with or involvement in any organization or entity with any financial interest or non-financial interest in the subject matter or materials discussed in this manuscript.

References

1. K. Ajay Kumar and C. Mallikarjuna, Wear Behavior of A356/ Al_2O_3 / MoS_2 Hybrid Nanocomposites, *Mater. Today Proc.*, 2021, **54**, p 409–414.
2. Y.A. Alghamdi, Z. Peng, Z. Almutairi et al., Assessment of Correlations for Minimum Fluidization Velocity of Binary Mixtures of Particles in Gas Fluidized Beds, *Powder Technol.*, 2021, **394**, p 1231–1239.

3. H.H. Xi, W.Q. Ming, Y. He et al., Unveiling the Fine Microstructure of Nanoscale Composite Particles Embedded in Brittle Si Phase in an Al-Si-Cu-Mg Alloy, *J. Alloys Compd.*, 2022, **906**, p 1123–1129.
4. Y. Wang, H. Toda, Y. Xu et al., In-Situ 3D Observation of Hydrogen-Assisted Particle Damage Behavior in 7075 Al Alloy by Synchrotron X-ray Tomography, *Acta Mater.*, 2022, **227**, p 758–768.
5. Z. Zhang and Y. Wang, Preparation of Nanocopper Particles on Al-Li Alloy by Salt Spray Droplets, *Mater. Lett.*, 2022, **315**, p 667–678.
6. Q. Niu, S. Li, Y. Chen et al., A Constitutive Model of Al/50 wt%SiP Composites Considering Particle Damage Effects, *Mater. Sci. Eng. A*, 2022, **836**, p 759–767.
7. X.C. Tong and A.K. Ghosh, Fabrication of In Situ TiC Reinforced Aluminum Matrix Composites, *J. Mater. Sci.*, 2001, **36**, p 4059–4069.
8. Z. Fan, Y. Wang, Y. Zhang et al., Grain Refining Mechanism in the Al/Al–Ti–B System, *Acta Mater.*, 2015, **84**, p 292–304.
9. C.-Y. Liu, G.-B. Teng, Z.-Y. Ma et al., Effects of Sc and Zr Microalloying on the Microstructure and Mechanical Properties of High Cu Content 7xxx Al Alloy, *Int. J. Miner. Metall. Mater.*, 2019, **26**(12), p 1559–1569.
10. Q. Yan, G. Chen, Z. Zhang et al., In-Situ Fabrication of Submicron α -Al₂O₃ Particle Reinforced AlSi₉Cu₃ Alloy Matrix Composites by TIG arc Process, *Mater. Res. Express*, 2019, **6**(6), p 489–497.
11. H. Su, W. Gao, Z. Feng et al., Processing, Microstructure and Tensile Properties of Nano-Sized Al₂O₃ Particle Reinforced Aluminum Matrix Composites, *Mater. Des. (1980–2015)*, 2012, **36**, p 590–596.
12. M. Karbalaei Akbari, O. Mirzaee and H.R. Baharvandi, Fabrication and Study on Mechanical Properties and Fracture Behavior of Nanometric Al₂O₃ Particle-Reinforced A356 Composites Focusing on the Parameters of Vortex Method, *Mater. Des.*, 2013, **46**, p 199–205.
13. Y. Zhao, S. Zhang, G. Chen et al., Effects of Molten Temperature on the Morphologies of In Situ Al₃Zr and ZrB₂ Particles and Wear Properties of (Al₃Zr+ZrB₂)/Al Composites, *Mater. Sci. Eng. A*, 2007, **457**(1–2), p 156–161.
14. S. Zhang, Y. Zhao, X. Cheng et al., High-Energy Ultrasonic Field Effects on the Microstructure and Mechanical Behaviors of A356 Alloy, *J. Alloys Compd.*, 2009, **470**(1–2), p 168–172.
15. S. Zhang, Y. Zhao, G. Chen et al., (Al₂O₃+Al₃Zr)/A356 Nanocomposites Fabricated by Magnetochemistry In Situ Reaction, *J. Alloys Compd.*, 2009, **475**(1–2), p 261–267.
16. Y. Zhao, S. Zhang, G. Chen et al., (ZrB₂+Al₂O₃+Al₃Zr)p/Al–4Cu Composite Synthesized by Magneto-Chemical Melt Reaction, *Mater. Sci. Eng. A*, 2008, **487**(1–2), p 1–6.
17. S. Mozammil, J. Karloopia, R. Verma et al., Effect of Varying TiB₂ Reinforcement and Its Ageing Behaviour on Tensile and Hardness Properties of In-Situ Al-45%Cu-xTiB₂ Composite, *J. Alloys Compd.*, 2019, **793**, p 454–466.
18. Y.-Y. Gao, F. Qiu, R. Geng et al., Effects of Nanosized TiCp Dispersion on the High-Temperature Tensile Strength and Ductility of In Situ TiCp/Al-Cu-Mg-Si Nanocomposites, *J. Alloys Compd.*, 2019, **774**, p 425–433.
19. R. Soundararajan, S. Sivasankaran, N. Babu et al., Appraisal of Tribological Properties of A356 with 20% SiC Composites Under Dry Sliding Condition, *J. Braz. Soc. Mech. Sci. Eng.*, 2020, **42**(3), p 7–16.
20. T. Tunçay, D. Özyürek, D. Dışınar et al., The Effects of Cr and Zr Additives on the Microstructure and Mechanical Properties of A356 Alloy, *Trans. Indian Inst. Met.*, 2020, **73**(5), p 1273–1285.
21. E. Erzi and M. Tiryakioğlu, A Simple Procedure to Determine Incoming Quality of Aluminum Alloy Ingots and Its Application to A356 Alloy Ingots, *Int. Metalcast.*, 2020, **14**, p 999–1004.
22. G. Sigworth, Understanding Quality in Aluminum Castings, *Int. Metalcast.*, 2011, **5**, p 7–22.
23. Z. Zhao, Y. Ma, H. Wan et al., Preparation and Tribological Behaviors of Polyamide-Imide/Polytetrafluoroethylene Lubricating Coatings Reinforced by In-Situ Synthesized CeO₂ Nanoparticles, *Polym. Test.*, 2021, **96**, p 58–69.
24. H. Wan, Y. Jia, Y. Ye et al., Tribological Behavior of Polyimide/Epoxy Resin-Polytetrafluoroethylene Bonded Solid Lubricant Coatings Filled with In Situ-Synthesized Silver Nanoparticles, *Prog. Org. Coat.*, 2017, **106**, p 111–118.
25. Y. Guo, D. Wang and S. Liu, Tribological Behavior of In Situ Ag Nanoparticles/Polyelectrolyte Composite Molecular Deposition Films, *Appl. Surf. Sci.*, 2010, **256**(6), p 1714–1719.
26. Y. Ma, H. Wan, Y. Ye et al., In-Situ Synthesis of Size-Tunable Silver Sulfide Nanoparticles to Improve Tribological Properties of the Polytetrafluoroethylene-Based Nanocomposite Lubricating Coatings, *Tribol. Int.*, 2020, **148**, p 12–21.
27. J.P. Singh, S. Singh, T. Nandi et al., Development of Graphitic Lubricant Nanoparticles Based Nanolubricant for Automotive Applications: Thermophysical and Tribological Properties Followed by IC Engine Performance, *Powder Technol.*, 2021, **387**, p 31–47.
28. P.J. Shi, H.L. Yu, H.M. Wang et al., Tribological Behaviour of Surface Modified Copper Nanoparticles as lubricating Additives, *Phys. Procedia*, 2013, **50**, p 461–465.
29. L.Z.Y. Jiao, Preparation and Wear Properties of (Al₃Zr+ZrB₂)p/2124 Composites Material with In-Situ Process, *Adv. Mater. Res.*, 2012, **600**, p 199–203.
30. L. Qi, Z. Li, Q. Zhang et al., Electromagnetic Stirring Control for Resistance Spot Welding of SiCp/Al Composites, *J. Manuf. Process.*, 2021, **68**, p 1271–1279.
31. M. Li, N. Omura, Y. Murakami et al., A Comparative Study of the Primary Phase Formation in Al–7 wt% Si and Al–17 wt% Si Alloys Solidified by Electromagnetic Stirring Processing, *Mater. Today Commun.*, 2020, **24**, p 667–679.
32. Y. Zhang, R. Li, P. Chen et al., Tuning the Microstructure Morphology and Genetic Mechanical Properties of 2219 Al Alloy with Ultrasonic Treatment, *J. Alloys Compd.*, 2020, **846**, p 675–685.
33. Y. Jia, D. Song, N. Zhou et al., The Growth Restriction Effect of TiCN Nanoparticles on Al-Cu-Zr Alloys via Ultrasonic Treatment, *Ultrason Sonochem.*, 2021, **80**, p 105829.
34. W. Wolf and E.M. Mazzer, The Influence of Particle Size and Heat Treatments on the Transformation Energies of a Gas Atomized Cu-Al-Ni-Mn Shape Memory Alloy, *Thermochim. Acta*, 2022, **707**, p 158–168.
35. H. Mao, C. Li, Y. Dong et al., The effect of Mn on particles morphology and property of 5 wt% TiB₂/Al-4.5Cu-0.4Mn alloys, *J. Alloys Compd.*, 2022, **904**, p 23–31.
36. K. Su, Q. Zhang, H. Hou et al., Properties and Microstructure Evolution of Unfired Al-Si Incorporated Al₂O₃-C Slide Plate Materials with Trace Nano-Al₂O₃ Particles, *Ceram. Int.*, 2021, **47**(23), p 33641–33650.
37. P. Zhang, X. Yue, Q. Zhang et al., Investigation on the Influence of SiC Particle Parameters on the Machinability of SiCp/Al Composite, *Vacuum*, 2021, **191**, p 56–67.
38. L. Yuan, J. Han, J. Liu et al., Mechanical Properties and Tribological Behavior of Aluminum Matrix Composites Reinforced with In-Situ AlB₂ Particles, *Tribol. Int.*, 2016, **98**, p 41–47.
39. R.G. Hidalgo-Hernandez, N. Plaza and O.M. Suárez, A Study on Tribological Characterization of Al-Cu-Mg-B Composites Subjected to Mechanical Wear, *Sci. Eng. Compos. Mater.*, 2014, **21**(3), p 566–576.
40. Y. Bai, Y. Guo, J. Li et al., Effect of Al₂O₃ Nanoparticle Reinforcement on the mechanical and High-Temperature Tribological Behavior of Al-7075 Alloy, *Proc. Inst. Mech. Eng. J. J. Eng. Tribol.*, 2016, **231**(7), p 900–909.
41. K. Yang, L. An and L. Cheng, Microstructure and Tribological Behavior of Al₂O₃ Particle Reinforced Al Matrix Composites Fabricated by Spark Plasma Sintering, *J. Wuhan Univ. Technol. Mater. Sci. Ed.*, 2019, **34**(5), p 1013–1017.
42. S. Agrawal, A.K. Ghose and I. Chakrabarty, Effect of rotary electromagnetic stirring during solidification of In-situ Al-TiB₂ composites, *Mater. Des.*, 2017, **113**, p 195–206.
43. H.B. Wu, J.Z. Li, D.F. Li et al., Microstructures and Properties of Spinning for Silicon Carbide Particle Reinforced Aluminum Composite, *Mater. Sci. Forum*, 2019, **944**, p 571–580.
44. V. Patil, S. Janawade, S.N. Kulkarni et al., Studies on Mechanical Behavior and Morphology of Alumina Fibers Reinforced with Aluminium-4.5% Copper Alloy Metal Matrix Composites, *Mater. Today Proc.*, 2021, **46**, p 99–106.
45. X.R. Li, W.B. Tang and J.T. Niu, Investigation on Joining Mechanism of SiC Particle Reinforced Aluminum Matrix Composite (Al/SiCp-MMC) by Resistance Spot Welding, *Mater. Sci. Forum*, 2011, **704–705**, p 1399–1405.
46. Y.L. Che, A. Shaban, G. Yu et al., Laser Beam Welding of SiC Particle Reinforced Aluminum Metal Matrix Composite, *Proc. Spie Int. Soc. Opt.*, 1999, **36**, p 36–42.
47. N. Kumar, R.K. Gautam and S. Mohan, In-Situ Development of ZrB₂ Particles and Their Effect on Microstructure and Mechanical Properties of AA5052 Metal-Matrix Composites, *Mater. Des.*, 2015, **80**, p 129–136.

48. H. Zhu, Z. Yu, B. Hua et al., Chemical Reaction Mechanism, Microstructural Characteristics and Mechanical Properties of In Situ (α -Al₂O₃+ZrB₂)/Al Composites, *Mater. Chem. Phys.*, 2017, **196**, p 45–51.
49. S.M. Dar, Y. Zhao, X. Kai, et al. Effect of External Pressure on the Microstructure and Mechanical Properties of In Situ (ZrB₂ + Al₂O₃/Al₃Zr)/6016 Nanocomposites. *Int. Metalcast.* (2022)
50. N. Ramadoss, K. Pazhanivel, A. Ganeshkumar, et al. Microstructural, Mechanical and Corrosion Behaviour of B4C/BN-Reinforced Al7075 Matrix Hybrid Composites. *Int. Metalcast.* (2022)
51. A.K. Yadav, V. Kumar, A. Ankit et al., Microstructure and Mechanical Properties of an In Situ Al 356-Mg₂Si-TiB₂ Hybrid Composite Prepared by Stir and Cooling Slope Casting. *Int. Metalcast.* (2022)
52. L. Jiao, B. Wang, Y. Zhao et al., Microstructure and Mechanical Properties of In Situ AlB₂/A356 Composites Under T6 Treatment. *Int. Metalcast.* (2022)
53. G. Li, T. Xu, H. Wang et al., Microstructure Study of Hot Rolling Nanosized In-Situ Al₂O₃ Particle Reinforced A356 Matrix Composites, *J. Alloys Compd.*, 2021, **855**(1), p 1571.
54. H. Ahmadian, A.M. Sadoun, A. Fathy et al., Utilizing a Unified Conceptual Dynamic Model for Prediction of Particle Size of Dual-Matrix Nanocomposites During Mechanical Alloying, *Powder Technol.*, 2023, **418**, p 118291.
55. G.S. Alsoruji, A.M. Sadoun, M.A. Elaziz et al., On the Prediction of the Mechanical Properties of Ultrafine Grain Al-TiO₂ Nanocomposites Using a Modified Long-Short Term Memory Model with Beluga Whale Optimizer, *J. Mater. Res. Technol.*, 2023, **23**, p 4075–4088.
56. A.M. Sadoun, I.M.R. Najjar, A. Fathy et al., An Enhanced Dendritic Neural Algorithm to Predict the Wear Behavior of Alumina Coated Silver Reinforced Copper Nanocomposites, *Alex. Eng. J.*, 2023, **65**, p 809–823.
57. I.R. Najjar, A.M. Sadoun, A. Fathy et al., Prediction of Tribological Properties of Alumina-Coated, Silver-Reinforced Copper Nanocomposites Using Long Short-Term Model Combined with Golden Jackal Optimization, *Lubricants*, 2022, **10**(11), p 277.
58. A.M. Sadoun, I.R. Najjar, G.S. Alsoruji et al., Utilization of Improved Machine Learning Method Based on Artificial Hummingbird Algorithm to Predict the Tribological Behavior of Cu-Al₂O₃ Nanocomposites Synthesized by In Situ Method, *Mathematics*, 2022, **10**(8), p 1266.
59. A. Mohamed, M.M. Mohammed, A.F. Ibrahim et al., Effect of Nano Al₂O₃ Coated Ag Reinforced Cu Matrix Nanocomposites on Mechanical and Tribological Behavior Synthesis by P/M Technique, *J. Compos. Mater.*, 2020, **50**, p 4921–4928.
60. M.S. El-Wazery, A. El-Desouky, O. Hamed et al., Electrical and Mechanical Performance of Zirconia-Nickel Functionally Graded Materials, *Int. J. Eng.*, 2013, **26**, p 375–382.
61. A.M. Sadoun, A.F. Meselhy and A.W. Deabs, Improved Strength and Ductility of Friction Stir Tailor-Welded Blanks of Base Metal AA2024 Reinforced with Interlayer Strip of AA7075, *Results Phys.*, 2020, **16**, p 102911.
62. A.M. Sadoun, A. Wagih, A. Fathy and A.R.S. Essa, Effect of Tool Pin Side Area Ratio on Temperature Distribution in Friction Stir Welding, *Results Phys.*, 2019, **15**, p 102814.
63. N. El Mahallawy, A. Fathy, M. Hassan, et al. Evaluation of Mechanical Properties and Microstructure of Al/Al–12%Si Multilayer via Warm Accumulative Roll Bonding Process. *J. Compos. Mater.* 2017
64. A.F. Meselhy and M.M. Reda, Investigation of Mechanical Properties of Nanostructured Al-SiC Composite Manufactured by Accumulative Roll Bonding, *J. Compos. Mater.*, 2019, **53**, p 3951–3964.
65. M. Elwan, A. Fathy, A. Wagih et al., Fabrication and Investigation on the Properties of Ilmenite (FeTiO₃)-Based Al Composite by Accumulative Roll Bonding, *J. Compos. Mater.*, 2020, **54**, p 1259–1271.

Publisher's Note Springer Nature remains neutral with regard to jurisdictional claims in published maps and institutional affiliations.

Springer Nature or its licensor (e.g. a society or other partner) holds exclusive rights to this article under a publishing agreement with the author(s) or other rightsholder(s); author self-archiving of the accepted manuscript version of this article is solely governed by the terms of such publishing agreement and applicable law.